nature materials

SUPPLEMENTARY INFORMATION

DOI: 10.1038/NMAT4971

In the format provided by the authors and unedited.

Realizing the classical XY Hamiltonian in polariton simulators

Natalia G. Berloff[1,2,*], Matteo Silva[3], Kirill Kalinin[1], Alexis Askitopoulos[3], Julian D. Töpfer[3], Pasquale Cilibrizzi[3], Wolfgang Langbein[4] and Pavlos G. Lagoudakis[1,3*]

[1]*Skolkovo Institute of Science and Technology Novaya St., 100, Skolkovo 143025, Russian Federation*

[2]*Department of Applied Mathematics and Theoretical Physics, University of Cambridge, Cambridge CB3 0WA, United Kingdom*

[3]*Department of Physics and Astronomy, University of Southampton, Southampton, SO17 1BJ, United Kingdom and*

[4]*School of Physics and Astronomy, Cardiff University, The Parade, Cardiff CF24 3AA, United Kingdom*

(Dated: June 20, 2017)

*correspondence address: n.g.berloff@damtp.cam.ac.uk,pavlos.lagoudakis@soton.ac.uk

Microcavity Sample

The semiconductor microcavity structure studied here is a planar, strain compensated 2λ GaAs microcavity with embedded InGaAs quantum wells (QWs). Strain compensation was achieved by $AlAs_{0.98}P_{0.02}$/GaAs DBR layers instead of the thin AlP inserts in the AlAs layers used in Ref. [S1] as their effective composition could be better controlled. The bottom DBR consists of 26 pairs of GaAs and $AlAs_{0.98}P_{0.02}$ while the top has 23 of these pairs, resulting in very high reflectance (>99.9%) in the stop-band region of the spectrum. The average density of hatches along the [110] direction was estimated from transmission imaging to be about 6/mm, while no hatches along the $[1\bar{1}0]$ direction were observed. Three pairs of 6 nm $In_{0.08}Ga_{0.92}As$ QWs are embedded in the GaAs cavity at the anti-nodes of the field as well as two additional QWs at the first and last node to serve as carrier collection wells. The large number of QWs was chosen to increase the Rabi splitting and keep the exciton density per QW below the Mott density [S2] also for sufficiently high polariton densities to achieve polariton condensation under non-resonant excitation. The strong coupling between the exciton resonance and the cavity mode is observed with a vacuum Rabi-splitting of $2\hbar\Omega \sim 8$ meV. A wedge in the cavity thickness allows access to a wide range of exciton-cavity detuning. All measurements reported here are taken at $\Delta \approx -5.5$ meV. The measured Q-factor is $\sim$ 12000, while the calculated bare cavity Q-factor, neglecting in-plane disorder and residual absorption, is $\sim$ 25000. As the emission energy of the InGaAs QWs is lower than the absorption of the GaAs substrate we can study the photoluminescence of the sample both in reflection and transmission geometry. The transmission geometry, which is not available for GaAs QWs, allows to filter the surface reflection of the excitation, and has been widely utilized to probe the features of polariton fluids [S3, S4] under resonant excitation of polaritons. Using real and reciprocal space imaging under non-resonant optical excitation, polariton condensation, and a second threshold marking the onset of photon lasing, i.e. the transition from the strong to the weak-coupling regime has been studied in this microcavity [S5].

Experimental setup

In the experiments described here the sample was held in a cold finger cryostat at a temperature of $T \approx 6\,\mathrm{K}$. Continuous wave excitation is provided by a Ti:Sapphire laser. We use non-resonant excitation from the epi side, and detect the emission from the substrate side, so that the excitation is filtered by the absorption of the GaAs substrate. The optical excitation, for all the measurements reported in this work, is at the first reflectivity minimum above the cavity stop band. The spatial profile of the excitation beam is modulated to a graph with Gaussian profiles at each vertex of approximatelly equal in diameter spots using a reflective spatial light modulator (SLM). We use a high numerical aperture microscope objective (NA = 0.65) to focus the spatially modulated beam to ∼1-2 μm in diameter at full width at half maximum (FWHM) excitation spots. The photoluminescence from the sample is collected in transmission geometry with ±25° collection angle, by a 0.42 NA microscope objective. Fourier (dispersion) imaging is performed by projecting the Fourier-space at the slit of a 300 mm spectrophotometer coupled a cooled charge coupled (CCD) device and using a 1200 grooves/mm with 50 μeV energy-resolution. The real-space spectral tomography is obtained with sub-micron optical resolution using a CCD camera imaging configuration through a tunable Fabry-Perot etalon with ∼ 20 μeV FWHM bandwidth.

Wavevector Tomography

The condensate wavevector, k_c, of the polariton Ising chains is measured using two dimensional Fourier-space imaging configuration. Figure S1(a-d) shows the false-grey scale images of the normalised photoluminescence intensity of the two dimensional Fourier-space from the Ising chain configurations of Fig.2(b-e) at condensation threshold. The outer ring in both images corresponds to k_c, whereas the inner fringes correspond to self-diffraction from the Ising chain. From Figure S1(a-d), k_c is $\approx 1.35\,\mu m^{-1}$, $\approx 1.37\,\mu m^{-1}$, $\approx 1.56\,\mu m^{-1}$ and $\approx 1.59\,\mu m^{-1}$ respectively.

Finding the expression for the coupling coefficients

The expression for the coupling coefficients J_{ij} given by Eq. (8) can be estimated based on the width of the Hankel transformation of the wavefunction of an individual condensate

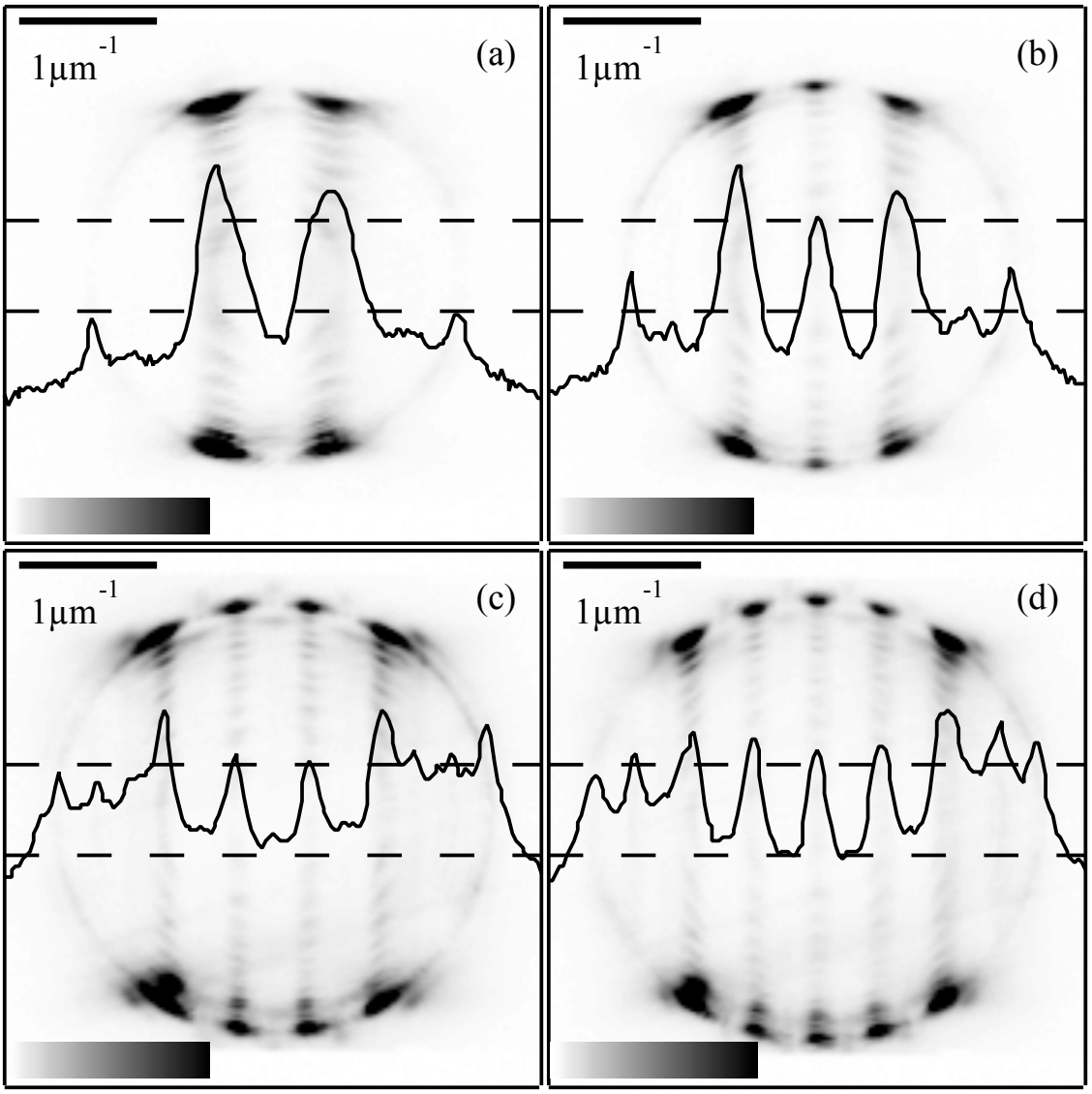

FIG. S1: (a) False-grey scale images of the normalised photoluminescence intensity of the two-dimensional Fourier-space from the Ising chain configurations of Fig.2(b-e). All images are saturated at 0.3 to improve the visibility of the interference fringes.

given by

$$\widehat{\Psi}(k) = 2\pi \int_0^\infty \sqrt{\rho(r)}\, \exp[ik_c r] J_0(kr) r\, dr. \tag{S1}$$

The density of the Hankel transformation, $|\widehat{\Psi}(k)|^2$, peaks at $k = k_c$ with the width, characterized by ϵ, inversely proportional to the width of the condensate density $\rho(r)$, which is set

by the width of the pumping profile $p(r)$. We, therefore, approximate $|\widehat{\Psi}(k)|^2$ by

$$|\widehat{\Psi}(k)|^2 \approx |\widehat{\Psi}(k_c)|^2 \frac{\mathrm{rect}(\frac{k-k_c}{\epsilon})}{\epsilon}. \tag{S2}$$

We integrate Eq. (8) using Eq. (S2) to get

$$\begin{aligned} J_{ij} \;=\; & \frac{1}{\pi}|\widehat{\Psi}(k_c)|^2 \Bigg[\left(\frac{k_c}{d_{ij}\epsilon} - \frac{1}{2d_{ij}} \right) J_1 \left(\frac{d_{ij}\epsilon}{2} - k_c d_{ij} \right) \\ & + \left(\frac{k_c}{d_{ij}\epsilon} + \frac{1}{2d_{ij}} \right) J_1 \left(\frac{d_{ij}\epsilon}{2} + k_c d_{ij}) \right) \Bigg]. \end{aligned} \tag{S3}$$

In the limit of $\epsilon \to 0$ we recover the $\delta-$function approximation $J_{ij} = k_c|\widehat{\Psi}(k_c)|^2 J_0(k_c d_{ij})/\pi$. The finite width of the Hankel transformation of the condensate wavefunction, as seen from Eq. S3, deviates the sign switching of J_{ij} from the zeros of the Bessel function. The criterion for the sign alternation of the coupling strength J_{ij} can be associated with the sign switching of $\cos(k_c d_{ij} + \phi)$, where ϕ is the system parameter dependent term.

Minimization of the XY Hamiltonian for sample configurations

We find the global minimum of the XY Hamiltonian directly for the sample configurations considered in our paper. For the lattice sites arranged in a square the phases relative to one fixed phase that we set equal to zero, $\theta_0 = 0$, minimize the XY Hamiltonian

$$\mathcal{H}_\square = -J(\cos\theta_{10} + \cos\theta_{12} + \cos\theta_{23} + \cos\theta_{30}) - J\delta(\cos\theta_{20} + \cos\theta_{13}), \tag{S4}$$

where we denoted δ to be the ratio of the coupling of the diagonal cites to the coupling of the neighboring sites. The coupling strength decays with the distance between sites, therefore, $|\delta| < 1$. If all couplings are ferromagnetic, $J, \delta > 0$, the minimum of $\mathcal{H}_\square$ is for $\theta_{i0} = 0$. If $J < 0$, there is a π phase difference between the neighboring sites $\theta_{10} = \pi, \theta_{20} = 0, \theta_{30} = \pi$ even for nonzero δ (as long as $|\delta| < 1$ is satisfied).

For a rhombus, consisting of two equilaterial triangles, the XY Hamiltonian becomes

$$\mathcal{H}_{rh} = -J(\cos\theta_{10} + \cos\theta_{20} + \cos\theta_{30} + \cos\theta_{12} + \cos\theta_{23}) - J\delta\cos\theta_{13}, \tag{S5}$$

where we associated $\theta_0 = 0$ with one of the sites along the shorter diagonal. δ in this case represents the ratio of the coupling along the long diagonal to that between the neighbours. While for an equilaterial triangle the XY Hamiltonian $\mathcal{H}_\triangle = -J(\cos\theta_{10} + \cos\theta_{20} + \cos\theta_{12})$,

$J < 0$ is minimized by $\theta_{i0} = \pm 2\pi/3$, the XY Hamiltonian (S5) is minimized by $\theta_{10} = \theta_{30} = \pi$, $\theta_{20} = 0$ as in the case of the square.

For three equilaterial triangles non-trivial winding around sites is again possible, since the XY Hamiltonian

$$\mathcal{H}_5 = -J(\cos\theta_{10} + \cos\theta_{20} + \cos\theta_{30} + \cos\theta_{40} + \cos\theta_{12} + \cos\theta_{23} + \cos\theta_{34}) \qquad \text{(S6)}$$

for $J < 0$ reaches its minimum at $\theta_{10} = -\theta_{40} = \pm 0.73\pi, \theta_{20} = -\theta_{30} = \mp 0.54\pi$, therefore, creating an alternating winding around each of the equilaterial triangles. Here we associated $\theta_0 = 0$ with the site that is connected to all other sites and neglected the interactions along two long diagonals. If the distances are close to the switching points between ferro- and antiferro- couplings the small deviation in the position of the sites may lead to an even more complex configurations as is illustrated on Fig. 5 of the main text.

Parameters of the numerical simulations

In our numerical simulation we used a Gaussian pumping profile that produces the same width of the condensate as in experiment (FWHM $2.6\mu m$) and choose the pumping intensity to obtain the correct outflow wavenumber for a single condensate. The common integration parameters used for all numerical simulations are, therefore, $g = 0.1, b = 1, \gamma = 0.3,\ \eta = 0.4,\ p = 9.5\exp(-0.4r^2)$. The numerical simulations were performed for various geometries and distances as the main text shows. For Fig. 3 we varied the distances between the nearest neighbors, so that $k_c d = 12.1, 15.3, 18.4, 16.8$ for Figs. 3a,b,c,d respectively. For Fig. 4 we used $k_c d = 19, 22.3, 24.9$ for Figs. 4a,b,c respectively. For Fig.5 we used $k_c d = 18.2 \pm 0.5$. All numerical simulations start from initial conditions with phases randomly distributed between the computational modes. The configuration with the largest number of particles, N, is chosen out of 100 runs for each pumping geometry.

[S1] Zajac, J. M., Clarke, E. & Langbein, W. Suppression of cross-hatched polariton disorder in GaAs/AlAs microcavities by strain compensation. *Appl. Phys. Lett.* **101**, 041114 (2012).

[S2] Houdre, R. *et al.* Saturation of the strong-coupling regime in a semiconductor microcavity: Free-carrier bleaching of cavity polaritons. *Phys. Rev. B* **52**, 7810 (1995).

[S3] Sanvitto, D. *et al.* All-optical control of the quantum flow of a polariton condensate. *Nature Photonics* **5**, 610 (2011).

[S4] Nardin, G. *et al.* Hydrodynamic nucleation of quantized vortex pairs in a polariton quantum fluid. *Nature Phys.* **7**, 635 (2011)

[S5] Cilibrizzi, P. *et al.* Polariton condensation in a strain-compensated planar microcavity with InGaAs quantum wells. *Appl. Phys. Letts.* **105**, 191118 (2014).